

## Suppression of Bulk Defects in Antimonide Superlattice Infrared Photodiodes

E. H. Aifer, E. M. Jackson<sup>1</sup>, B. R. Bennett, I. Vurgaftman,  
J. R. Meyer, and G. G. Jernigan  
Naval Research Laboratory,  
Washington, DC 20375-5347, U.S.A.  
<sup>1</sup>SFA Inc., Largo, MD 20774, U.S.A.

### ABSTRACT

While physical properties of ideal antimonide superlattices (ASL) indicate that they should significantly outperform mercury cadmium telluride (MCT) based infrared photodiodes for low dark current applications in the long and very long wave-infrared (LWIR and VLWIR), this potential has not yet been fully realized. Even though measured Auger and tunneling rates in ASL's are reduced as predicted, overall carrier lifetimes remain much shorter, and dark currents much higher than expected. The large carrier losses are the result of defects in the ASL structure, with contributions measured from large bulk defects and surface channels along mesa sidewalls, and the remaining component believed to be due to midgap states.

In this presentation we report on several studies of epitaxial growth parameters and their influence on defect formation. X-ray photoelectron spectroscopy analysis of oxide desorption from GaSb substrates shows the presence of both antimony and gallium oxides, along with their decomposition and desorption behavior with anneal temperature. A study of buffer growth shows that defect density and size are critically dependent on growth temperature, with an optimal growth window between 480 and 500 °C. Side-by-side GaSb buffer growths on vicinal ((100) + 1° (111)) and flat (100) substrates show that while growing on vicinal material can suppress mound formation, it does not yield epilayers as flat as can be obtained on (100) substrates grown under optimal conditions. Finally, the ratio of As to In flux during superlattice growth can be used to tune the lattice parameter both above and below that of GaSb, with strain-related defects appearing when the mismatch reaches roughly 0.1%.

### INTRODUCTION

Antimonide superlattices (ASLs), composed of binary (GaSb/InAs) or ternary antimonide layers ( $\text{In}_x\text{Ga}_{1-x}\text{Sb}/\text{InAs}$ ), are potentially an important material system for long-wave and very-long-wave infrared (LWIR 8-14  $\mu\text{m}$  & VLWIR 14-24  $\mu\text{m}$ ) focal plane arrays. The interest in ASL material is due to key advantages it offers over the current material of choice,  $\text{Hg}_{1-x}\text{Cd}_x\text{Te}$  (MCT).

Smith and Mailhot first proposed that type II antimonide superlattices could be used to realize an artificial direct narrow-gap semiconductor with comparable optical absorption to MCT [1]. The type II band alignment of the ASL (Fig. 1) results in quantum confinement of electrons in the InAs conduction band and holes in the GaSb valence band, producing electron and hole minibands with a positive IR gap. In the binary structure (Fig. 1(a)), the IR gap is tuned by adjusting the thickness of the layers. This is potentially a problem for long wavelength devices since the electron-hole wavefunction overlap gets smaller with increased layer thickness, although high efficiency has been observed in a device with a 16  $\mu\text{m}$  cutoff [2]. In ternary ASLs

(Fig.1 (b)), strain in the  $\text{In}_x\text{Ga}_{1-x}\text{Sb}$  hole quantum wells reduces the energy gap and therefore allows thinner layers with larger wavefunction overlaps to be employed at the same cut-off wavelength.

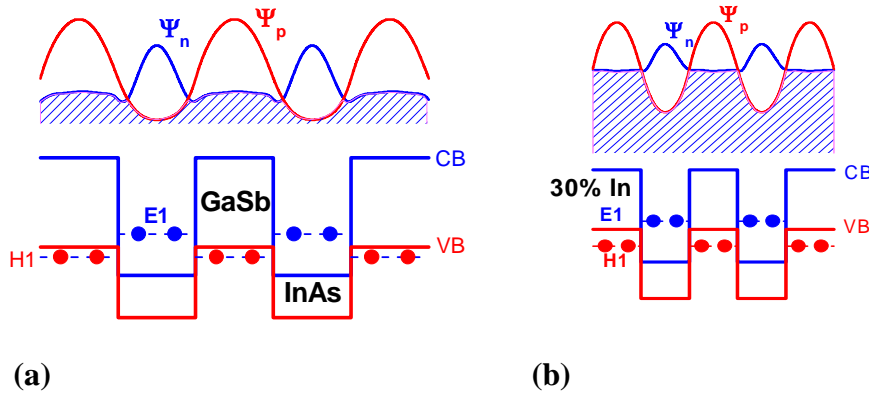


**FIG. 1.** (a) 10ML/10ML Binary ASL, and (b) and 6ML/6ML ternary ASL with same energy gap but with enhanced electron-hole wavefunction overlap.

Because they are direct narrow-gap semiconductors that generate minority carrier current under IR illumination, ASL and MCT photodiodes have several orders of magnitude lower dark current due to thermal generation than majority carrier photodetectors such as quantum well infrared photodetectors (QWIPs) or extrinsic semiconductors [3]. Auger recombination processes that limit carrier lifetimes in bulk MCT materials at higher temperature are strongly suppressed in ASLs [4,5]. This is a function of the strained-layer superlattice bandstructure, in which the availability of light-hole to heavy-hole transitions resonant with the band-gap is greatly reduced. ASLs are also much better suited to VLWIR applications than MCT, where band-to-band tunneling processes limit operation to the short edge of the VLWIR spectrum. This is due to the exponential dependence of tunneling current  $J_T$  on effective mass  $m^*$  and energy gap  $E_g$  [6].

$$J_T = C_1 m^{*1/2} \cdot \exp(-C_2 \cdot m^{*1/2} E_g^{3/2}) \quad (1)$$

Since the ASL growth-axis effective mass ( $m_{ASL}^* \sim .03 m_0$ ) is about a factor of three larger than that of MCT ( $m_{MCT}^* \sim .01 m_0$ ), ASL photodiodes can operate at significantly longer wavelengths.

### **Material challenge**

Within the last few years, substantial progress has been made toward realizing the potential of infrared photodiodes based on ASLs. While performance characteristics of individual devices have begun to exhibit levels comparable to MCT [7], these results are still well below theoretical limits. Studies correlating bulk defect density [8] and sample surface roughness [9] with increased dark current have shown that some of this performance deficit is due to the presence of bulk defects. As the performance of individual devices continue to improve, and efforts turn to array development, eliminating the occurrence of bulk defects will become increasingly important.

In this work, we describe several studies aimed at identifying the relationship between several key growth parameters and the occurrence of bulk defects, such as the ones exhibited in Figure 2. Included are investigations of pre-growth oxide desorption, GaSb buffer growth, substrate vicinality and As/In ratio during superlattice growth.

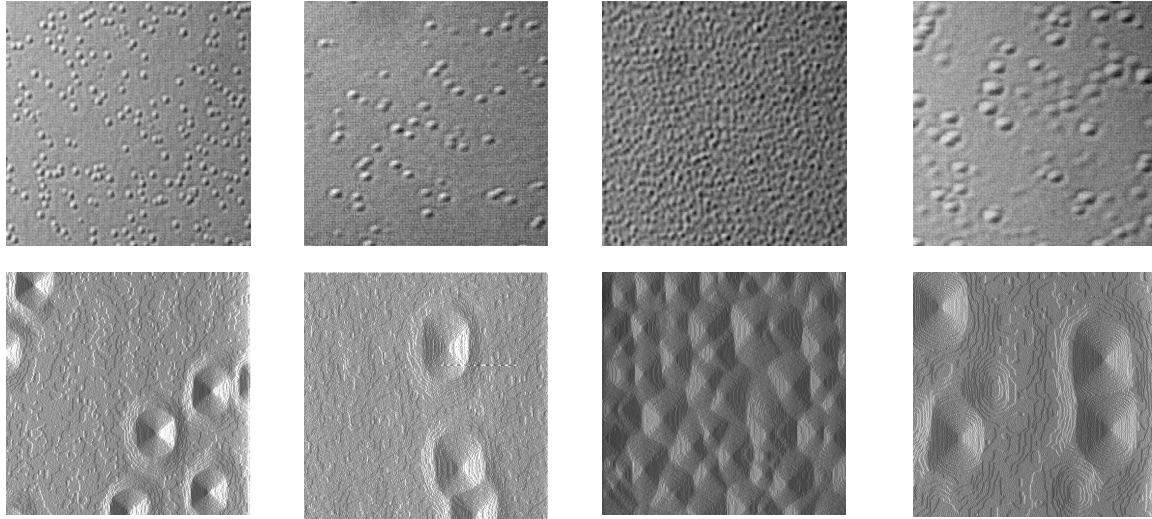


**FIG. 2. (Upper)** 50x50  $\mu\text{m}$  micrographs of 0.5  $\mu\text{m}$  GaSb buffers grown on (100) GaSb substrates with defect densities ranging from  $10^6$  to  $10^8/\text{cm}^2$ . **(Lower)** Corresponding 10x10  $\mu\text{m}$  AFM derivative images.

## EXPERIMENTAL

### Oxide desorption

Prior to epitaxial growth, wafers must be annealed to desorb surface oxides. The composition and thickness of the oxide layer are dependent on the preparation and storage procedures of the substrate vendor. In the case of GaSb substrates, “epi-ready” surface treatments can vary considerably and therefore optimal anneal procedures are unique to each supplier. In this study, x-ray photoelectron spectroscopy (XPS) was used to evaluate annealing procedures on (100) GaSb substrates obtained from Wafer Technology (UK).

New wafers sealed in nitrogen filled bags were loaded into a Vacuum Generator V80 MBE growth chamber within minutes of unpacking, and brought to base pressure of  $2 \times 10^{-10}$  mbar. Individual samples were ramped to annealing temperatures in approximately five minutes, and quenched after five minutes of heat treatment. The samples were then transferred in-vacuo to an adjacent ESCALab MKII system for XPS analysis. XPS was performed using a Mg x-ray (1253.6 eV), and spectra were taken of the Ga(2p), Sb(3d), Ga(3d), Sb(4d), and O(1s) peaks. Five minute anneals were performed at 250, 400, 500 and 550  $^{\circ}\text{C}$  without antimony flux.

XPS traces for the region of the antimony doublet Sb(3d) and O(1s) are shown for low temperature anneals at left in Fig. 3(a), and for high temperature anneals at right in Fig.3(b). The “as-delivered” surface signal is given by the solid red trace of Fig. 3(a) which has antimony oxide peaks (SbOx) that are larger than the elemental Sb peaks. After a five minute 250  $^{\circ}\text{C}$

anneal (blue dashed trace Fig. 3(a)), the SbOx peaks decrease, accompanied by a complimentary increase in the elemental antimony signal, marking the *decomposition* of SbOx. At 400 °C (black dash-dotted trace, Fig.3(a)), the antimony oxide signal has vanished and the remaining oxygen

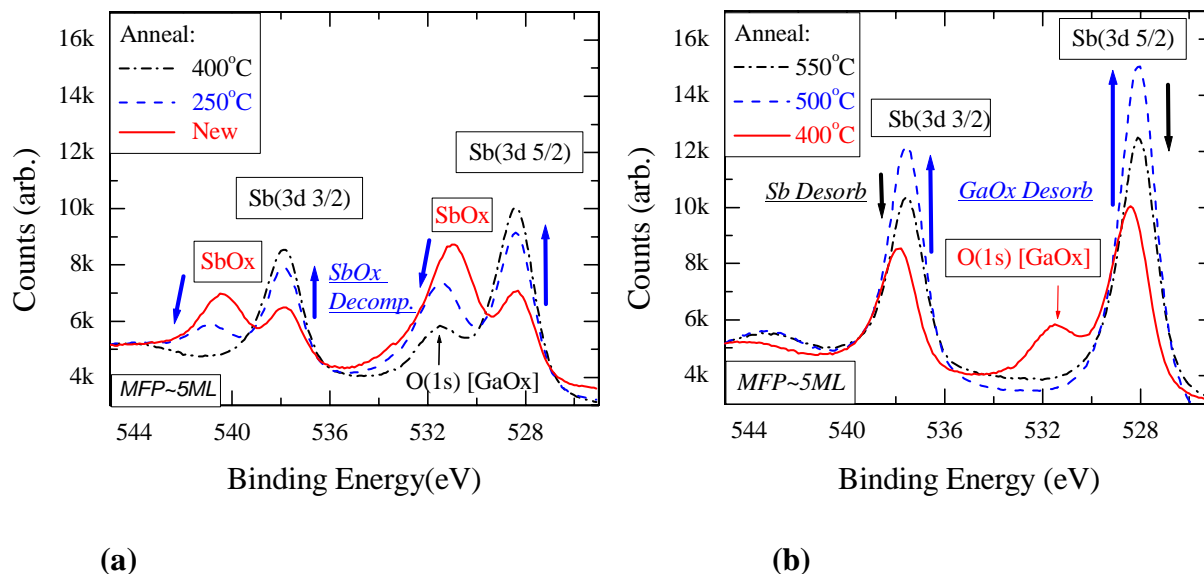


**FIG. 3.** XPS traces about the Sb(3d) doublet for low **(a)** and high **(b)** anneal temperatures.

(1s) peak comes from an oxide of gallium, most likely Ga<sub>2</sub>O<sub>3</sub>. In the blue dashed trace of Fig. 3(b), we see the gallium oxide peak vanish and the elemental antimony peaks significantly increase, as a result of a 500 °C anneal. In comparison to an antimony reference sample, the surface at 500 °C has a layer of excess antimony (most likely from the SbOx decomposition). Finally, after a treatment of 550 °C, the antimony peaks (blue dash-dotted Fig. 3(b)) *decrease*, representing a loss in antimony.

The XPS signals for the Ga(2p) region is shown in Fig. 4. The mean free path of the Ga(2p) electrons ( $L_{MFP}$ ) is only about 6 Å or 2 ML [10], so that the Ga(2p) peak is much more surface sensitive than that of the Sb(3d) doublet, which have  $L_{MFP} \sim 15$  Å. In anneals up to 400 °C (Fig. 4(a)), the GaOx peak is seen to increase without shifting toward elemental gallium, corresponding to the decomposition of SbOx discussed above. The attenuation of the Ga(2p) GaOx signal implies that initially the top two or three monolayers of oxide is composed of at least a significant portion, if not all, antimony oxide.

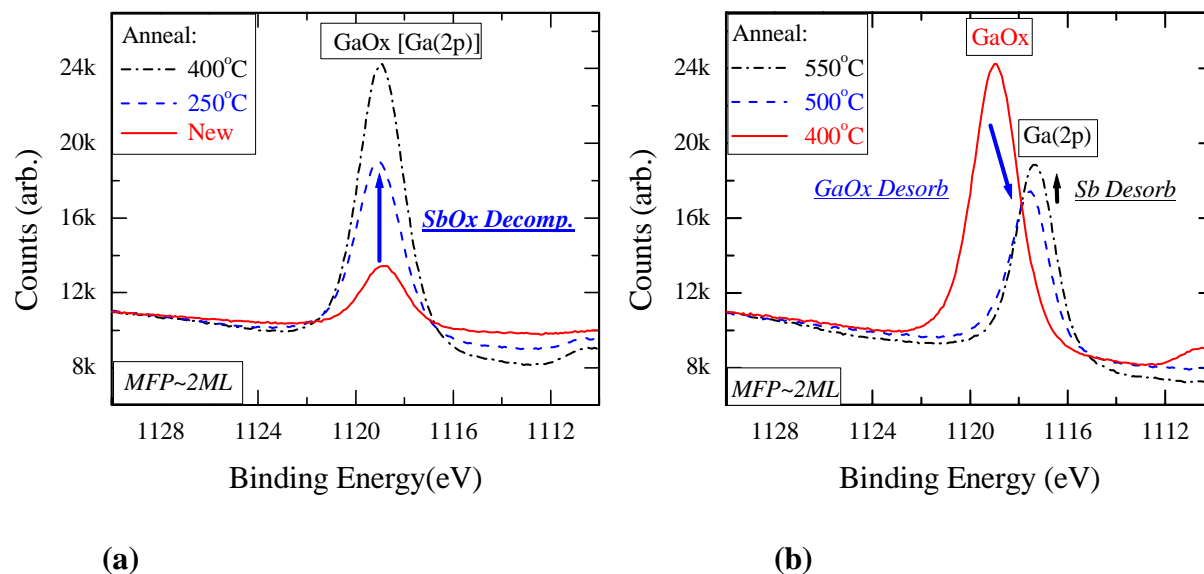


**FIG. 4.** XPS traces of Ga(2p) peak for low (a) and high (b) anneal temperatures.

After a 500 °C anneal (blue dashed trace Fig. 4(b)), the GaOx peak is replaced by an elemental peak of about half the size. Unlike the antimony oxide, which decomposes above 250 °C leaving excess antimony behind, the gallium oxide desorbs entirely from the surface. We have confirmed this by comparing the large reduction from oxidized to elemental gallium in the surface sensitive Ga(2p) peak to the negligible change observed in the bulk Ga(3d) peak. From the changes in the Sb(3d) peaks (Fig. 3(b)) and the Ga(2p) peaks (Fig. 4(b)) as a function of the 500 °C anneal, the GaOx layer is expected to be about 15 Å thick.

The 550 °C anneal produces a small increase in the Ga(2p) peak, just as it results in a somewhat larger loss in the Sb(3d) peaks. Using elemental antimony and gallium standards, peak-fitting analysis indicate that the surface remains stoichiometric at 550 °C, so that the change most probably reflects a loss in the excess antimony obtained from the decomposition of the antimony oxide.

In sum, the substrates we obtained from Wafer Technology are coated with a combination of antimony and gallium oxides about 5-7 monolayers in total thickness. The top layers are either mixed GaOx/SbOx or pure SbOx, with the remaining layers pure GaOx. The antimony oxide decomposes under an anneal of 250 °C, leaving excess antimony behind. The gallium oxide is removed by a 500 °C anneal, but it may be necessary to go up to 550 °C to remove the excess antimony.

### **Growth parameter influence on homo-epitaxy**

A series of 0.5 μm thick undoped GaSb buffers were grown on “flat” (100) GaSb substrates to investigate the influence of pre-growth oxide-desorption temperature, desorption time, and growth temperature on defect density and size. The buffers were grown on quarter sections of 2”

substrates to allow multiple growths on individual substrates to eliminate variation in starting material.

The growths were performed in a Riber MBE system using a cracked-antimony (Sb<sub>2</sub>) source. The growth rate, set by a constant gallium flux, was 1 monolayer/sec (ML/s). Beam flux was measured before and after growths with a standard hot filament flux gauge. Sample temperature was monitored using a thermocouple radiatively coupled to the substrate at a distance of less than 1 mm. The chamber was equipped with an in-situ reflectance high-energy electron diffraction (RHEED) system to determine sample surface structure.

Substrates were loaded and out-gassed for about 30 min at 370 °C, then transferred to the growth chamber, which had a base pressure of 10<sup>-7</sup> mtorr. Sample temperatures were first ramped quickly to within 20 degrees of where RHEED spots were expected to appear and then brought up in steps of 10 and 5 °C, allowing at least 3 minutes to equilibrate at each step. The RHEED system was monitored continuously during this fine temperature scan, and the thermocouple value at which the first RHEED spot appeared was designated T<sub>RHEED</sub>. The sample was then ramped at 5 °C/min to a target oxide desorption temperature (T<sub>XO</sub>) specified relative to T<sub>RHEED</sub>, and held at that temperature for a specified anneal time, Δt<sub>XO</sub>. The substrate was then cooled to the growth temperature (T<sub>GR</sub>) and was allowed to equilibrate while the Sb flux was adjusted to the desired level. After buffer growth, the sample was cooled slowly to a temperature below the 5X to 3X surface reconstruction (T<sub>5X3</sub>). The 5x to 3x transition temperature was then measured as temperature was slowly increased. The sample was then quenched and Sb flux measured. Absolute temperature calibration was achieved by correlating T<sub>5X3</sub> and the measured antimony flux, with the experimentally determined reconstruction phase diagram [11]. The uncertainty in temperature (+/- 4.6 °C) was obtained by a least square fit of T<sub>RHEED</sub> vs. T<sub>5X3</sub>.

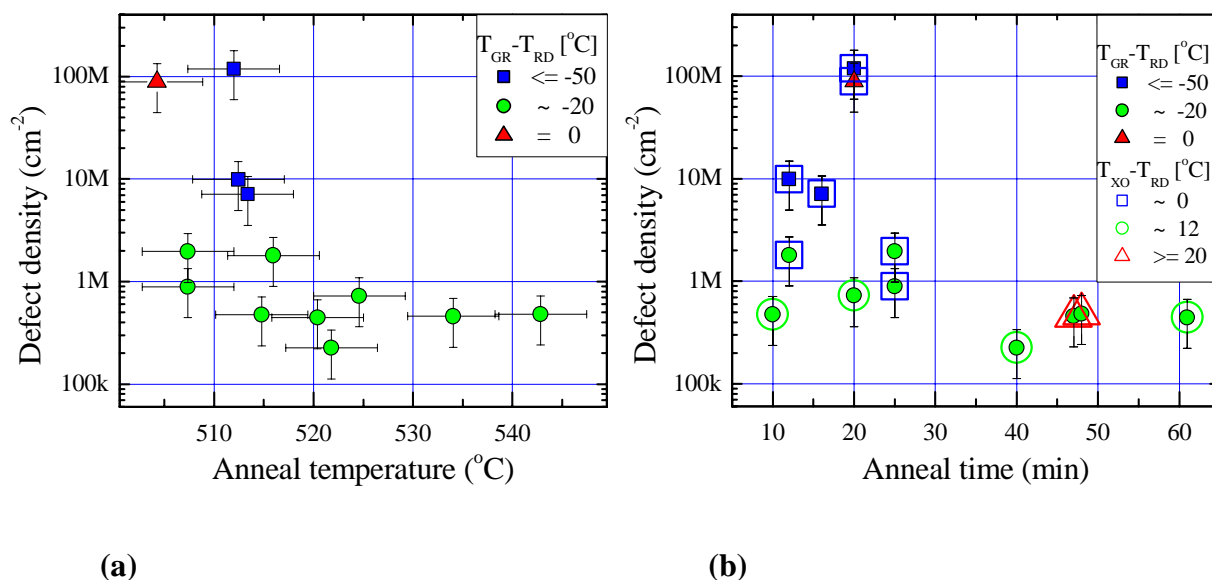


**FIG. 5. (a)** Defect density vs. oxide desorption temperature, T<sub>XO</sub>. **(b)** Defect density vs. anneal time, Δt<sub>XO</sub>.

The dependence of defect density on oxide desorption parameters is shown in Fig. 5. Samples were annealed at temperatures ranging from where RHEED spots first appeared, about 505 °C, up to 545 °C. Over this range, defect density can be seen to be independent of anneal temperature, for samples with growth temperature around 20 °C below  $T_{\text{RHEED}}$  (solid green circles Fig. 5(a)). The anneal appears inadequate only for samples grown “hot” at  $T_{\text{RHEED}}$  (red triangles), or “cold” at least 50 °C below  $T_{\text{RHEED}}$  (blue squares). Similarly, defect counts are seen to be independent of anneal times when samples are grown around 20 °C below  $T_{\text{RHEED}}$  (solid green circles in Fig. 5(b)), regardless of desorption temperature as indicated by the open figures. On the other hand, samples on the extremes of growth temperature (solid blue squares at least 50 °C below  $T_{\text{RHEED}}$ , solid red triangle grown at  $T_{\text{RHEED}}$ ) always have at least one to two orders of magnitude higher defect counts.

Evidently, growth temperature is the critical parameter in defect generation and growth as can be seen in Fig. 6. With the dotted line as a guide for the eye, one can see that a narrow temperature window exists around 490 °C where defect density (solid green circles) approaches within an order of magnitude of that quoted by the substrate vendor for the etch-pit dislocation density. In complimentary fashion, defect *size* exhibits a maximum in the same growth temperature region (solid triangles).

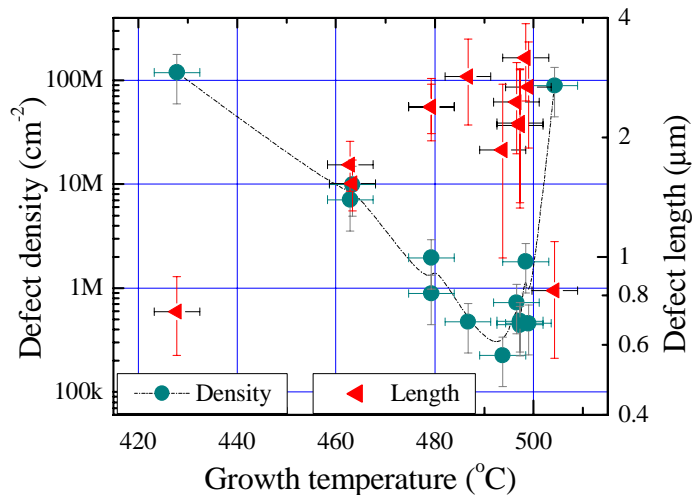


**FIG. 6.** Defect density and size dependence on growth temperature.

This behavior is clearly illustrated in Fig. 7, in which micrograph (upper) and AFM (lower) images are displayed above their respective growth temperatures.

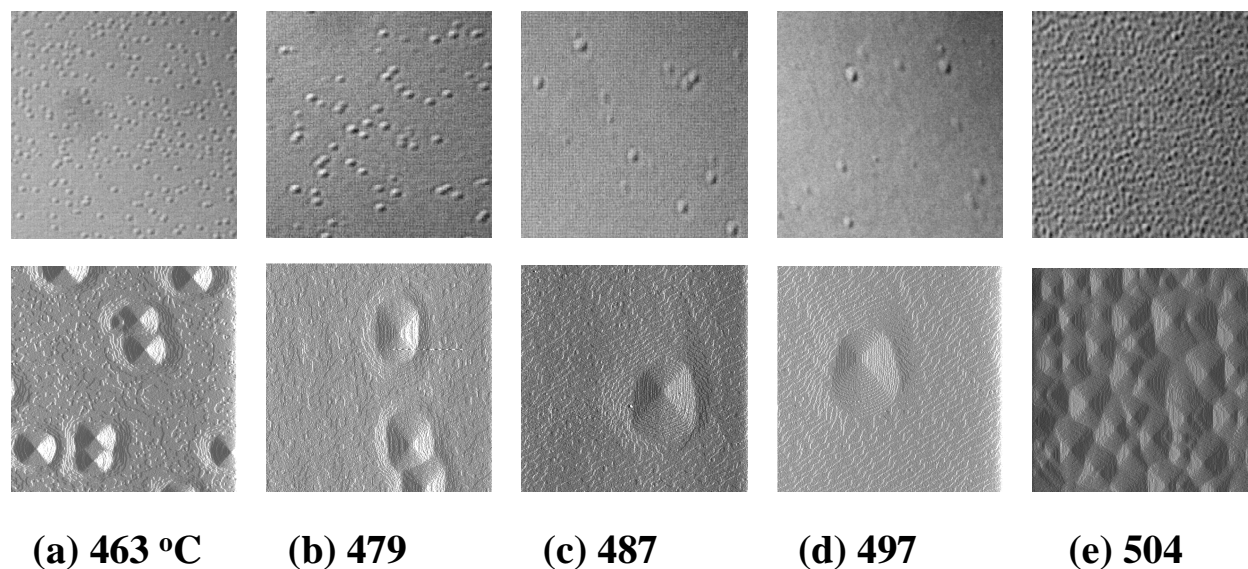


**FIG. 7. (Upper)** Micrographs of  $50 \times 50 \mu\text{m}$  regions of  $0.5 \mu\text{m}$  GaSb buffers grown at temperatures indicated below AFMs. **(Lower)** AFM derivative images of upper samples.  $10 \times 10 \mu\text{m}$  regions with 1 ML terraces.

Despite the density and size variations with temperature, the defects maintain a similar pyramidal structure (Fig. 8 (left)). The bases of the pyramids are rectangular, oriented with sides parallel to the  $\{011\}$  cleavage planes and elongated in the  $[0\bar{1}1]$  direction.

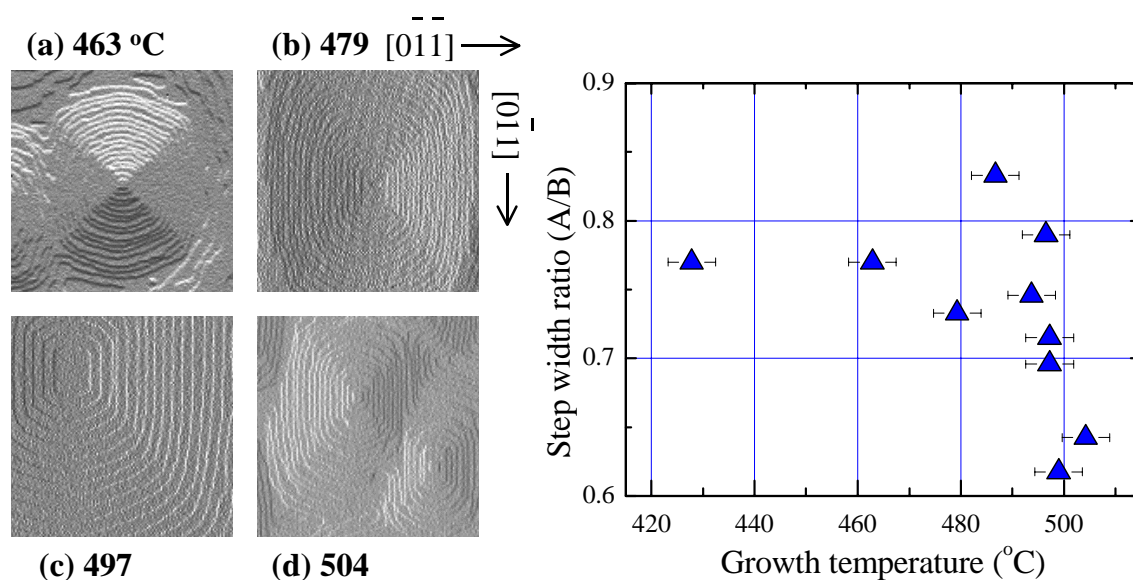


**FIG. 8.** Temperature dependence of anisotropic step structure on pyramid defects. **(Left)**  $2 \times 2 \mu\text{m}$  AFM derivative images of defects showing 1-ML steps on sidewalls for growth temperatures from  $463 \text{ }^\circ\text{C}$  to  $504 \text{ }^\circ\text{C}$  (a-d). **(Right)** Ratio of *A-step* to *B-step* width vs. growth temperature.

The anisotropy of the defects is reflected in the step structure on the sides of the pyramids (Fig. 8 (left)). The steps running parallel to the  $[0\bar{1}1]$  direction, *A-steps*, range from 30 to 90 nm in width while those parallel to  $[0\bar{1}\bar{1}]$  direction, or *B-steps*, range from 40 to 130 nm. The ratio of *A-step* width to *B-step* width stays at roughly three-fourths for growth temperatures up to 495 °C (Fig. 8 (right)). Around 500 °C, as defect density goes back up and size goes down, the B-steps appear to shrink more slowly than the A-steps, although the uncertainty in this measurement increases rapidly in this regime.

### **Substrate Vicinality and Homoepitaxy**

Substrate vicinality is known to have dramatic impact on mound formation. In a previous study, based on side-by-side buffer growths on vicinal and flat substrates, it was observed that pyramid formation during GaSb buffer growth was effectively suppressed on substrates oriented  $1^\circ$  toward (111) A [13].

We repeated the experiment, this time at the higher temperatures indicated by our study of defect dependence on growth temperature. A first set of one-half micron thick GaSb buffers was grown at 480 °C (Fig. 9(a)) near optimal growth temperature, and a second set was grown 35 °C higher in temperature (Fig. 9(b)).

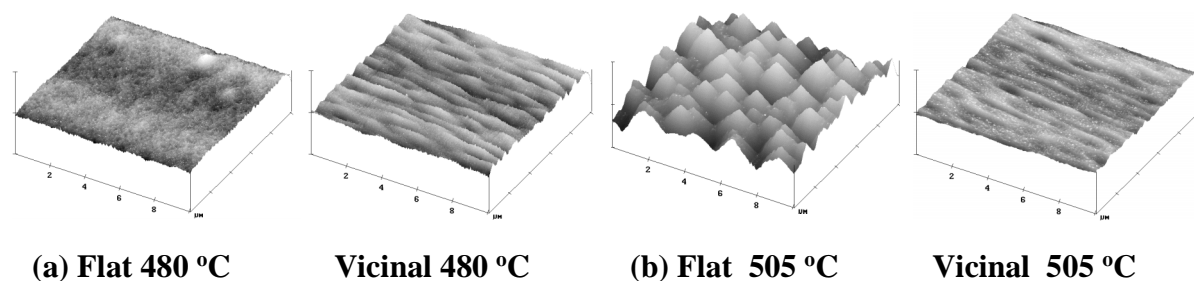


**FIG. 9.**  $10 \times 10 \mu\text{m}$  AFMs of GaSb buffers grown side-by-side on “flat” (100) and vicinal ( $1^\circ$  toward (111)A) substrates. **(a)** Grown near optimal temperature. **(b)** Grown “hot”. Vertical full scale = 10nm.

As in the earlier work, the vicinal substrates proved effective in preventing the formation of pyramidal mounds, this time at elevated temperatures (Fig. 9(b)). However, neither vicinal sample compares well with growth on the (100) substrate at 480 °C (Fig. 9(a)), nor with the other optimized growths discussed earlier. The vicinal substrates yield surfaces with dense undulations, having characteristic length scales similar to small isolated mound defects. It is plausible that the small terrace width of the  $1^\circ$  vicinals, measured to be about 20 nm, inhibit pyramids growth by disrupting the formation of the larger terraces found on defects. In so doing however, they also inhibit planar growth that is possible in defect free regions of growths on (100) substrates.

## Influence of As/In flux ratio on superlattice growth

Finally we looked at parameters influencing superlattice growth, and report here on the effects of varying the As to In flux ratio on superlattice morphology. Superlattices consisting of forty periods of 13 ML InAs on 13 ML GaSb were grown over 0.3  $\mu\text{m}$  GaSb buffers on vicinal substrates ( $1^\circ$  toward (111) A) at  $400^\circ\text{C}$ . Interfaces were forced to be InSb-like by controlling the shutter sequence [13]. The structure was expected to have a relaxed lattice constant 0.062% smaller than the substrate.

Both the buffer and superlattices were grown at a rate of 0.5 ML/s. The GaSb growth rate was calibrated from RHEED oscillations during buffer growth. The InAs growth rate was calibrated on separate substrates prior to superlattice growth. In all cases, the Sb:Ga flux ratio was 2:1. The As:In flux ratio was varied from 1.5:1 to 3.5:1 where we define a flux by the growth rate it can sustain. Thus, a flux of 1 is just sufficient to sustain a growth rate of 1 ML/s on GaSb InAs. The As valve was closed during buffer growth but open throughout the superlattice growth.

In Fig. 10 it can be seen that the changes in flux ratio had a significant effect on superlattice morphology. In the upper figures, micrographs of  $50\times 50\mu\text{m}$  regions show high densities of large defects only for an As/In flux ratio of 1.5 (a). The corresponding  $10\times 10\mu\text{m}$  AFM surface plots below indicate additional roughening between defects particularly at the highest As flux levels (e).

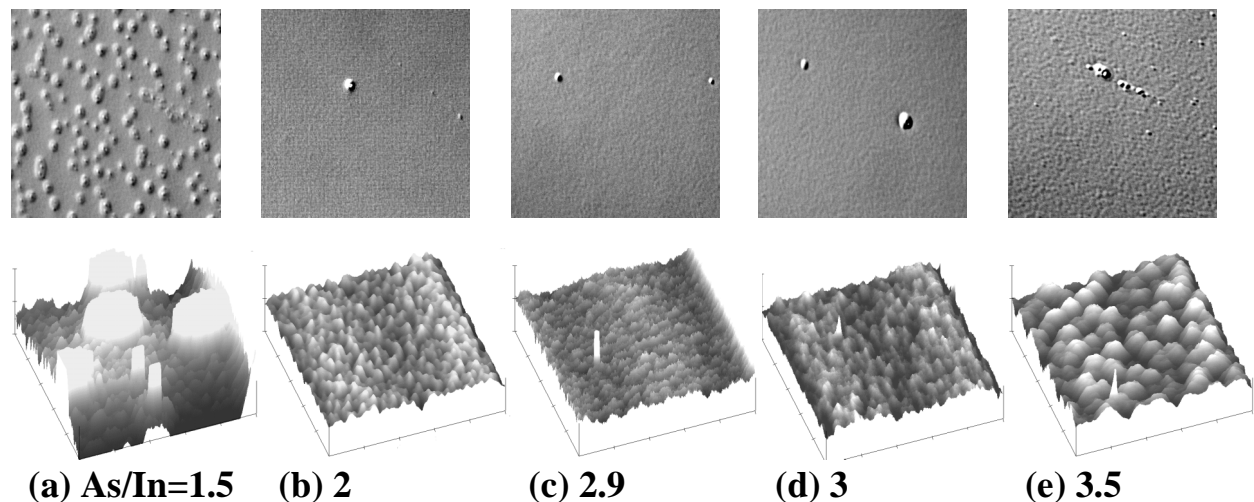


**FIG. 10 (upper)** Micrographs of  $50\times 50\mu\text{m}$  regions of 40 period InAs/GaSb 13/13 ML superlattices. **(lower)** Corresponding AFM surface plots of  $10\times 10\mu\text{m}$  regions with 5 nm full vertical scale. As/In flux ratios given below AFM images.

From x-ray diffraction measurements, it is evident that the As/In ratio has significant impact on the heterostructure lattice constant (Fig. 11). The sample with a flux ratio of 1.5 is under large compressive strain due to a lattice constant 0.14% larger than that of the substrate (Fig. 11(a) solid black trace), which produces the large density defects seen in Fig. 10(a). At higher flux ratios, the strain becomes tensile as the heterostructure lattice constant becomes smaller than that of the substrate. In Fig. 11(b), one can see that the average lattice constant varies approximately

linearly with As flux. From Vegard's law, we estimate that at the lowest As flux the InAs layer must contain at least 6% Sb. This is a minimum since it assumes that there is no As in the GaSb layer. Similarly, at the highest As flux, the GaSb layer must contain at least 5% As.

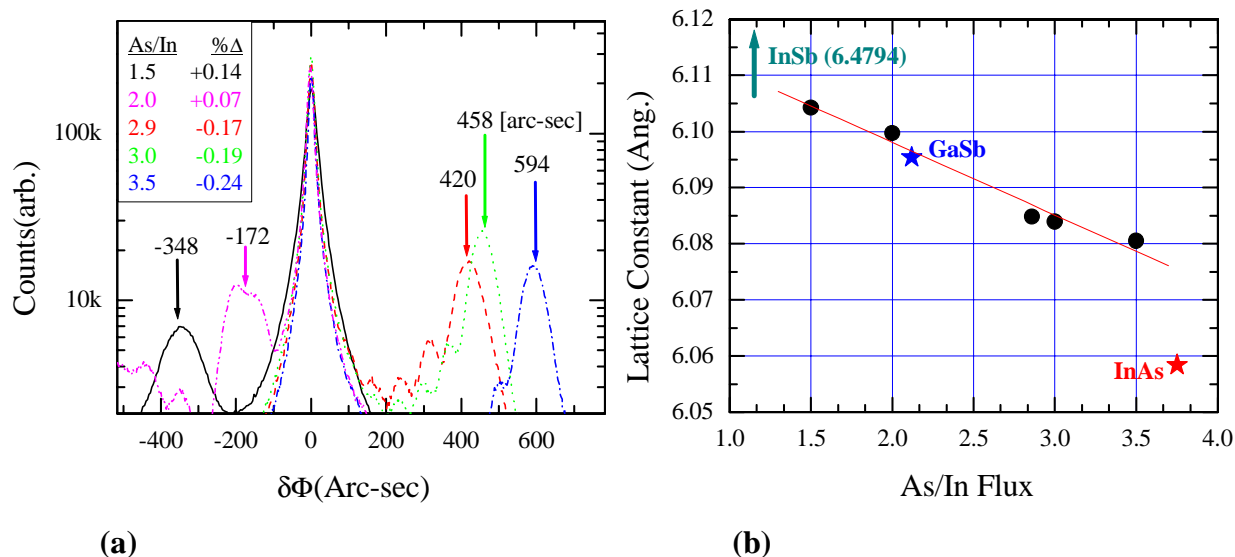


**FIG. 11.**(a) Central portion of X-ray diffraction scan showing shift of superlattice diffraction peaks relative to substrate. Associated lattice mismatch in legend. (b) Lattice constant as a function of As/In ratio.

Previous work has shown that much of the Sb in the InAs layers is excess from the GaSb surface reconstruction while the As in the GaSb is primarily from the background As flux during GaSb growth [14,15]. The GaSb surface reconstruction has about 1.6 ML of Sb depending on the Sb flux[16]. Since the InSb interface bonds absorb 1 ML of Sb, the amount of Sb available to be incorporated into the InAs is about 0.6 ML. This corresponds to about 5% Sb in a 13 ML InAs layer, which is about the amount estimated above for the sample with the lowest As flux, where it was assumed no As incorporated in the GaSb layer.

## CONCLUSIONS

We have investigated several aspects of ASL growth, including pre-growth oxide desorption, optimizing GaSb buffer growth and the effect of modifying the As/In flux ratio. XPS studies of oxide desorption of epi-ready GaSb substrates, identified a mixture of antimony and gallium oxides on starting material about 15 Å thick that desorbs in several stages, requiring anneals of up to 550 °C to obtain a stoichiometric GaSb surface. A study of GaSb homo-epitaxy showed there to be critical dependence on growth temperature for minimizing pyramid defects, and identified an optimal growth window around 490 °C. Vicinal substrates (1° toward (111)A) proved effective in suppressing large defect formation under non-optimized growth conditions, but the vicinal growths are rough relative to optimized growth on flat (100) GaSb substrates. Finally, the lattice constant of GaSb/InAs superlattices can be effectively tuned via the arsenic to indium flux ratio.

## ACKNOWLEDGMENTS

The authors would like to thank Dr. B. Z. Noshov for helpful discussion. Work supported by the Office of Naval Research.

## REFERENCES

1. D. L. Smith and C. Mailhiot, *J. Appl. Phys.* **62** 2545 (1987).
2. H. Mohseni, M. Razeghi, G. J. Brown, and Y. S. Park, *Appl. Phys. Lett.* **78**, 2107 (2001)
3. M. A. Kinch, *J. Elec. Mat.* **29** 809 (2000).
4. C. H. Grein, P. M. Young, and H. Ehrenreich, *Appl. Phys. Lett.* **61** 2905 (1992).
5. E. R. Youngdale, J. R. Meyer, C. A. Hoffman, F. J. Bartoli, C. H. Grein, P. M. Young, H. Ehrenreich, R. H. Miles, and D. H. Chow, *Appl. Phys. Lett.* **64** 3160 (1994).
6. S. M. Tze, *Physics of Semiconductor Devices*, 2<sup>nd</sup> ed. (John Wiley and Sons, New York, 1969) p.98.
7. F. Fuchs, U. Weimer, W. Pletschen, J. Schmitz, E. Ahlswede, M. Walther, J. Wagner, and P. Koidl, *Appl. Phys. Lett.* **71**, 3251 (1997).
8. E. H. Aifer, B. R. Bennett, B. Z. Noshov, M. E. Twigg, I. Vurgaftman, J. R. Meyer, J. R. Waterman, and M. Goldenberg, *2001 MSS Specialty Groups on Passive Sensors; Camouflage, Concealment and Deception; Detectors; and Materials*, ed. IRIA Center, Vienna, VA, filename MTC02EA.pdf (2001).
9. F. Fuchs, L. Bürkle, W. Pletschen, J. Schmitz, M. Walther, H. Güllich, N. Herres, and S. Müller, *Proc. SPIE* **3794**, 41 (1999).
10. M. P. Seah and W. A. Dench, *Surface and Interface Analysis*, **1**, 2 (1979)
11. A. S. Bracker, M. J. Yang, B. R. Bennett, J. C. Culbertson, and W. J. Moore, *J. Cryst. Growth*, **220**, 384 (2000).
12. B. Z. Noshov, B. R. Bennett, E. H. Aifer, and M. Goldenberg, *J Cryst. Growth.* **236**, 155 (2002).
13. B. R. Bennett, B. V. Shanabrook, R. J. Wagner, J. L. Davis, and J. R. Waterman, *Appl. Phys. Lett.* **63**, 949 (1993).
14. B.Z. Noshov, B.R. Bennett, L.J. Whitman, and M. Goldenberg, *J. Vac. Sci. Technol. B* **19**, 1626 (2001).
15. Qianghua Xie, J. E. Van Nostrand, J. L. Brown, and C. E. Stutz, *J. Appl. Phys.* **86**, 329 (1999).
16. J. Steinshnider, J. Harper, M. Weimer, C. H. Lin, S. S. Pei, and D. H. Chow, *Phys. Rev. Lett.* **85**, 4562 (2000).